ADVANCED QUANTUM TECHNOLOGIES
www.advquantumtech.com

Emerging Weyl Semimetal States in Ternary TaP_xAs_{1-x} Alloys: Insights from Electronic and Topological Analysis

Samira Sadat Nourizadeh, Aminollah Vaez, and Daryoosh Vashaee**

This study presents a thorough analysis of the electronic structures of the TaP_xAs_{1-x} series of compounds, which are of significant interest due to their potential as topological materials. Using a combination of first principles and Wannier-based tight-binding methods, this study investigates both the bulk and surface electronic structures of the compounds for varying compositions ($x = 0, 0.25, 0.50, 0.75, 1$), with a focus on their topological properties. By using chirality analysis, (111) surface electronic structure analysis, and surface Fermi arcs analysis, it is established that the TaP_xAs_{1-x} compounds exhibit topologically nontrivial behavior, characterized as Weyl semimetals (WSMs). The effect of spin–orbit coupling (SOC) on the topological properties of the compounds is further studied. In the absence of SOC, the compounds exhibit linearly dispersive fourfold degenerate points in the first Brillouin zone (FBZ) resembling Dirac semimetals. However, the introduction of SOC induces a phase transition to WSM states, with the number and position of Weyl points (WPs) varying depending on the composition of the alloy. For example, TaP has 12 WPs in the FBZ. The findings provide novel insights into the electronic properties of TaP_xAs_{1-x} compounds and their potential implications for the development of topological materials for various technological applications.

1. Introduction

Nontrivial topological states have attracted a great deal of attention in condensed matter physics due to their unique and exotic properties. One such state is the topological Weyl semimetal (WSM), which hosts fermionic quasiparticles in the bulk and anomalous gapless states at the boundary.[1,2] In WSMs, the valence and conduction bands touch each other at the twofold degenerate Weyl points (WPs) with linear dispersion.[1] It is well known that WPs may only arise if a material breaks either inversion symmetry (IS) or time-reversal symmetry (TRS). In a system with TRS and IS breaking, WPs at a $\vec{k}$ point must have a partner at a $-\vec{k}$ point with the same chirality, so the minimum nonzero number of WPs is four.[3–5] These systems normally appear in alloys with strong spin–orbit coupling (SOC) and non-centrosymmetric properties. In a system with IS and TRS breaking, the minimal number of WPs is two. These systems typically appear in alloys containing magnetic elements. The topology of the WPs can be verified through the Berry curvature,[6] which shows wave function entanglement between the valence and conduction bands. A WP acts as a monopole of the Berry curvature with fixed chirality and behaves as a source (sink) with positive (negative) chirality. A consequence of the monopole trait of the WPs is the existence of Fermi arcs. The exotic Fermi arc surface states form open curves in k-space, ending at the projection of the WPs on the surfaces.[7–9] The total chirality of the WPs must be zero; thus, each pair of WPs must have opposite chirality.[6,10,11] These unusual features of WSMs lead to novel phenomena and potential applications such as unconventional quantum oscillations in magnetotransport,[14] negative magnetoresistance under parallel electric and magnetic fields,[15] and unusual quantum interference effects in tunneling spectroscopies.[12,13]

The discovery of Weyl fermions in the quantum field theory has long been known, but the experimental evidence was not established until their observation in TaAs and its isoelectronic counterparts.[21,22] The topology of WSMs is characterized by the presence of WPs where the valence and the conduction bands touch each other at twofold degenerate points with linear dispersion.[1] In nonmagnetic materials such as TaAs, TaP, NbAs, and NbP, band inversion in the mirror-invariant planes leads to gapless nodal rings in the energy–momentum dispersion

S. S. Nourizadeh, A. Vaez
Faculty of Physics
University of Isfahan
Isfahan 8174673441, Iran
E-mail: vaez@phys.ui.ac.ir
D. Vashaee
Department of Electrical and Computer Engineering
NC State University
Raleigh, NC 27606, USA
E-mail: dvashae@ncsu.edu
D. Vashaee
Department of Materials Science and Engineering
NC State University
Raleigh, NC 27606, USA

The ORCID identification number(s) for the author(s) of this article can be found under https://doi.org/10.1002/qute.202300072

DOI: 10.1002/qute.202300072

in the absence of the SOC.[23] However, in the presence of the SOC, gaps open in the mirror planes, leading to WPs off the mirror planes.[23–25] The TaAs compound hosts 24 WPs distributed throughout the first Brillouin zone (FBZ),[16,21,26] and their Weyl cones in the bulk and Fermi arcs on the surface were identified using first-principles calculations and angle-resolved photoemission spectroscopy (ARPES) data.[21,23]

Other WSMs have been predicted using the same approach as TaAs, including the orthorhombic $MoTe_2$,[27] $Hg_{1-x-y}Cd_xMn_yTe$,[28] $SrSi_2$,[29] LaAlGe,[30] the hexagonal or Heusler structures of NaAuTe,[31] and HfIrX (X = As, Sb, Bi).[32] Some of these WSMs were confirmed experimentally with Fermi arc observations,[8,21,24,33–35] while others were confirmed only based on first-principles calculations.[36]

Alloying is a well-established method for manipulating the structure and electronic or topological properties of a material. In this study, we investigate the TaP_xAs_{1-x} (x = 0, 0.25, 0.50, 0.75, 1) series of compounds with enantiomorphic chiral space group P1 (NO.1) by combining first-principles and Wannier-based TB methods. Our study provides new insights into the electronic and topological properties of these alloys, including chirality analysis, (111) surface electronic structure, and surface Fermi arcs analysis. Our results demonstrate the potential of these compounds to serve as novel topological materials with various technological applications.

In Section 2, we present our methodology, which combines first-principles and Wannier-based TB methods. We then proceed to describe the structural and electronic properties of the alloys with and without SOC considerations in Section 3.1, followed by the topological properties of the alloys in Section 3.2. Finally, we present our conclusions and results in Section 4.

2. Methodology

The primary calculations are performed in the density functional theory (DFT)[37] with the full-potential linearized augmented plane wave (LAPW) using the Wien2k package.[38] The topological characters in bulk and the surface are investigated using the Wannier90 package based on the Maximally Localized Wannier Functions (MLWFs)[39] and using the WannierTools package.[40]

The structural and electronic properties are calculated using the Wien2k package based on the generalized gradient approximation (GGA) in the Perdew–Burke–Ernzerhof (PBE) exchange-correlation functional.[41] The energy convergence criterion for the self-consistent calculations is set to 10^{-5} eV, and the magnitude of the largest force acting on the atoms to less than 0.1 (eV Å^{-1}). The plane wave expanded cutoff of the wave function is set to $K_{max} = \frac{9.50}{R_{MT}}$ (a.u.)$^{-1}$ in the interstitial region, in which R_{MT} represents the smallest atomic muffin-tin radius (R_{MT}) for each alloy. The value of the R_{MT} for different atoms in each alloy is presented in **Table 1**. The cutoff vector for the Fourier expansion of the charge density and the potential function is chosen as G_{max} = 13.0(Ry)$^{1/2}$. A 6 × 6 × 2 k-mesh is used to sample the FBZ for all alloys. All the electronic structure calculations are calculated in the present and the absence of the SOC for comparison.

We generate the atomic-like Wannier functions for Ta-5d, As-4p, and P-4p orbitals to calculate the topological states using the Wannier90 package. The Wannier90 package uses the Wien2k output data of the wave functions to generate the tight-binding (TB) Hamiltonian. The band structure of the alloys, with the generated TB Hamiltonian, is fitted with the band structures obtained by the Wien2k package. The alloys with the P1 (No. 1) space group do not have IS. To investigate the topological properties and predict the existence of the WSM in the alloys, we cannot use the usual parity conditions and symmetry properties;[24] hence, we use the WannierTools package to calculate the topological properties. WannierTools is based on the MLWFs TB model. Another software, like the Wannier90, usually generates the TB Hamiltonian. The WannierTools can classify the topological phases by calculating the Wilson loop.[42] It also can search and identify the exact positions of the WPs in the FBZ. This code calculates the Berry phase around a closed momentum loop and the chirality of nodal points in the FBZ. It also produces the surface state spectrum, including the surface projected band structure, based on the iterative Greens function method.[43,44]

Table 1. Lattice constants, minimum atomic muffin-tin radius (R_{MT}), total energy (E_t), and formation energy (E_f) of TaP_xAs_{1-x} (x = 0, 0.25, 0.50, 0.75, 1) alloys.

Alloy	a [Å]	c [Å]	R_{MT} [Å]	E_t [eV]	E_f [eV]
TaAs	4.837	12.095	Ta = 2.37 As = 2.25	−286 196.061	−0.057
$TaP_{0.25}As_{0.75}$	4.800	11.986	Ta = 2.35 As = 2.23 P = 2.00	−278 520.176	−0.007
$TaP_{0.5}As_{0.5}$	4.754	11.918	Ta = 2.37 As = 2.25 P = 2.02	−270 844.292	−0.013
$TaP_{0.75}As_{0.25}$	4.709	11.832	Ta = 2.39 As = 2.12 P = 2.05	−263 168.425	−0.002
TaP	4.675	11.767	Ta = 2.50 P = 1.98	−255 492.552	−0.199

3. Result and Discussion

3.1. Structural and Electronic Properties

The TaP_xAs_{1-x} alloys are characterized by a triclinic Bravais lattice with an enantiomorphic space group P1 (No. 1). To construct these alloys, a 2 × 2 × 2 supercell of TaAs compound is used, with As atoms substituted by P atoms in appropriate amounts for each x%. It is worth noting that there are multiple possible positions for the substitution of P atoms in the supercell. To determine the optimal positions for different compositions of x = 0, 0.25, 0.5, 0.75, and 1, we used two criteria: symmetry of the supercell and energy minimization. For instance, using these criteria for the x = 0.25%, As atoms in the (0.70, 0.70, 0.41) and (0.08, 0.58, 0.66) positions are replaced by P atoms (as shown by green circles in **Figure 1**b). Figure 1a–c illustrates the 2 × 2 × 2 supercell of TaAs, it is corresponding primitive cell, and it is FBZ with high symmetry paths, respectively.

All electronic calculations were done after fitting the energy–volume curves by the Brich–Murnaghan equation of state (EOS),[45] which is an accurate EOS to obtain the optimized

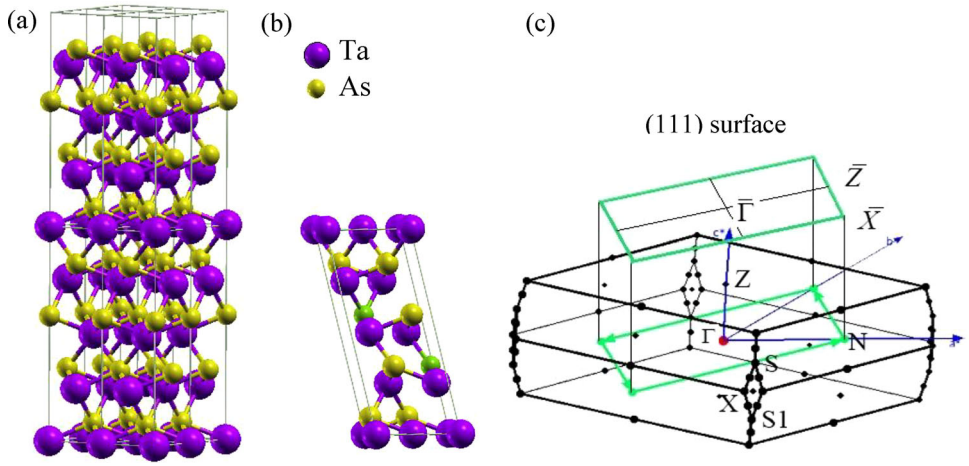

Figure 1. a) Conventional unit cell of the $2 \times 2 \times 2$ TaP_xAs_{1-x} supercell, b) triclinic primitive unit cell of TaP_xAs_{1-x} with As atoms substituted by P atoms for the $x = 0.25$ composition, represented by green circles, and c) FBZ of TaP_xAs_{1-x} with high symmetry k-point paths for band structure calculations. The green rectangular plane corresponds to the (111) surface.

parameters, like the lattice parameters. The calculated equilibrium lattice parameters are presented in Table 1.

The formation energy (E_f) of all alloys has been calculated to study their stability. The E_f of the TaP_xAs_{1-x} ($x = 0.25, 0.50, 0.75$) is defined by Equation (1)

$$E_f\left(TaP_xAs_{1-x}\right) = E_t\left(TaP_xAs_{1-x}\right) - xE_t\left(TaP\right) - (1-x)\,E_t\left(TaAs\right) \quad (1)$$

where $E_t(TaP_xAs_{1-x})$, E_t(TaP), and E_t(TaAs) are the ground-state total energy of the TaP_xAs_{1-x}, TaP, and TaAs, respectively (Table 1). The E_f of TaP(As) is calculated by Equation (2)

$$E_f\left(TaP\left(As\right)\right) = E_t\left(TaP\left(As\right)\right) - \frac{E_t\left(Ta\right)}{n} - \frac{E_t\left(P\left(As\right)\right)}{n} \quad (2)$$

where E_t (Ta) and E_t (P(As)) are the ground-state energy of Ta or P(As), respectively, and n is the number of Ta or P(As) atoms in the primitive cells of TaP(As) (Figure 1b). The calculated E_f of the TaP_xAs_{1-x} alloys for different values of x are presented in Table 1.

It is seen that the E_f is negative for all alloys, indicating that they are thermodynamically stable. Furthermore, TaP is the most stable structure among all the alloys. The electronic band structure and the density of states (DOS) calculations are essential because most of the physical properties of materials are related to them. Hence, the band structure of the alloys along different high symmetry paths (Z-S-S1-Γ-Z-N-Γ) in the FBZ and the DOS without (with) SOC were calculated as shown in **Figure 2** (**Figure 3**). To investigate the effect of x on the electronic properties of the alloys, we also calculated the total and atomic DOS for different x values without (with) SOC as shown in Figure 2 (Figure 3). The results of atomic DOS in both Figures 2 and 3 reveal that the valence and the conduction bands near the Fermi level are dominated by the 5d orbital of Ta atoms (d-Ta).

Without the SOC consideration, as illustrated in Figure 2, the valence and conduction bands overlap in the Z-S-S1-Γ path, while they are fully gapped in the Γ-Z-N-Γ path. For example, for the case of $x = 0.25$, Figure 2b clearly shows the overlapped valence and conduction bands in the Z-S-S1-Γ path, indicated by the yellow box. Furthermore, band inversion is observed in all alloys, as indicated by the crossing of four bands near the Fermi level along the Z-S-S1-Γ path. This inversion is confirmed by the lower energy of the d_{z^2} orbital compared to the d_{xz} and d_{yz} orbitals, contrary to the usual order of the d orbitals. Figure 2f shows the d orbital order for TaP, with the inverted bands along the S-S1 path. Notably, each crossing point of the conduction and valence bands in the Z-S-S1-Γ path has a fourfold degeneracy composed of d_{z^2} and $d_{x^2-y^2}$ orbitals and d_{xz} and d_{yz} orbitals, and displays linear energy dispersion in their vicinity.

Figure 3 shows the effect of SOC on the electronic structure of the TaP_xAs_{1-x} alloys. In this case, all crossing points along the Z-S-S1-Γ path are found to be gapped, for all alloys. This is unlike the case without the SOC, where crossing points are not gapped. For instance, Figure 3b displays the gapped valence and conduction bands in the Z-S-S1-Γ path for $x = 0.25$. The bandgaps along the Z-S-S1-Γ path have minimum values of 26, 30, 26, 35, and 37 meV for $x = 0$, $x = 0.25$, $x = 0.50$, $x = 0.75$, and $x = 1.0$, respectively. Notably, the bandgaps increase with increasing x, except for the $x = 0.50$ alloy.

3.2. Topological Properties

Without considering the SOC, the nontrivial topological properties of alloys are indicated by the band inversion and the four-fold degenerate crossing points. These alloys exhibit a double-WSM state with fourfold degenerate crossing points along the Z-S-S1-Γ. Although these degeneracies resemble Dirac points, they are not protected by point group symmetry and are lifted by SOC. Therefore, they are considered accidental degeneracies, and the materials are not considered DSMs. The topological features of alloys without SOC consideration are similar, but there are differences in the numbers and positions of the fourfold degenerate points in the first Brillouin zone. The positions of these points are even functions of $\vec{k}$ due to time-reversal symmetry, with each point having a partner in $-\vec{k}$ in the first Brillouin zone.

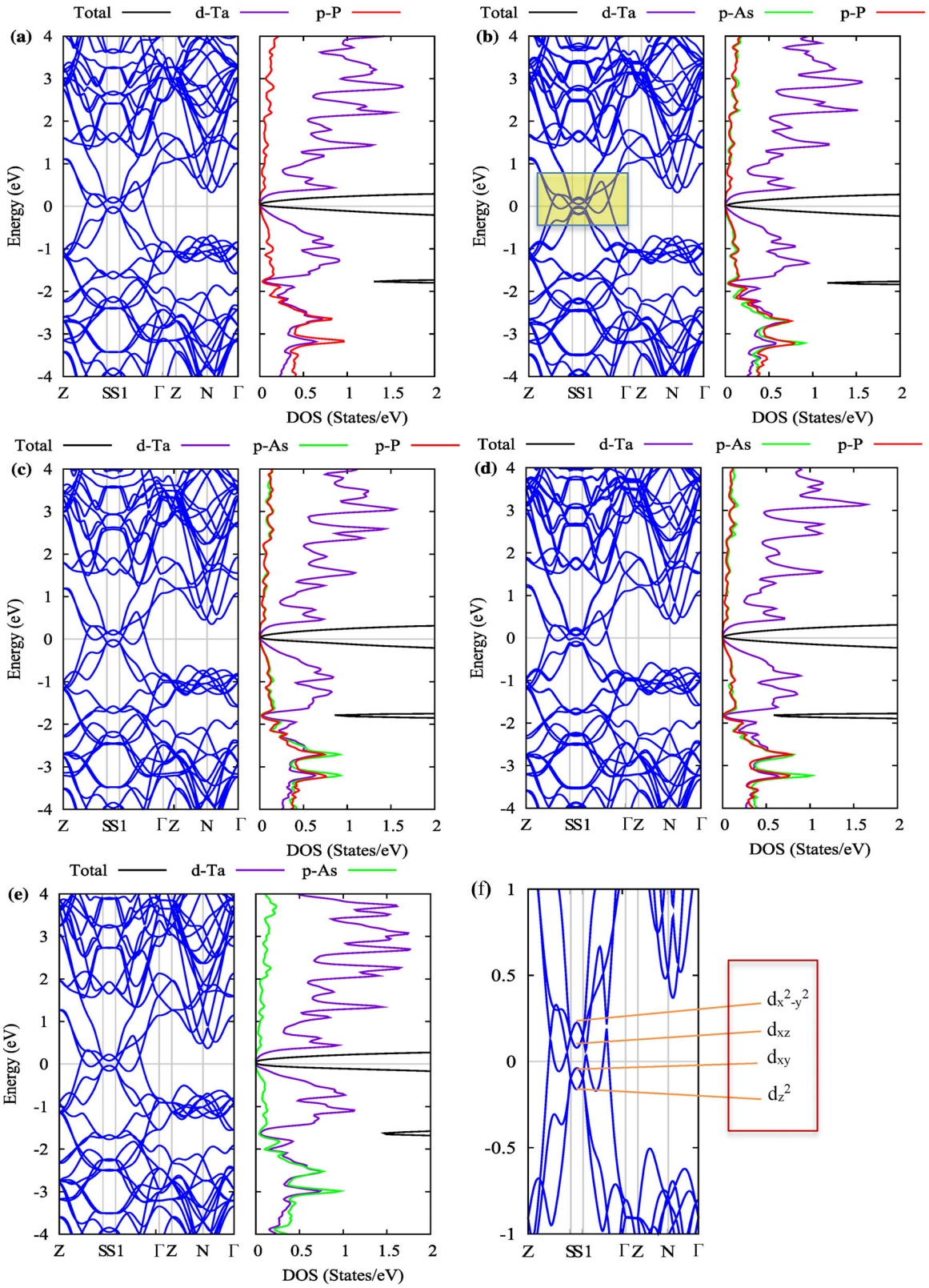

Figure 2. Band structures and density of states for the TaP_xAs_{1-x} compounds without considering the SOC. a) Band structure for TaAs, b) band structure for $TaP_{0.25}As_{0.75}$ with overlapped valence and conduction bands along the Z-S-S1-Γ path, as highlighted in the yellow box, c) band structure for $TaP_{0.5}As_{0.5}$, d) band structure for $TaP_{0.75}As_{0.25}$, and e) band structure for TaP. f) Band structure of TaP from −1.0 to 1.0 eV, demonstrating the inverted d orbital order between the d_{z^2} and the d_{xz}/d_{yz} orbitals along the S-S1 path highlighted in the red box, confirming the band inversion in the alloy.

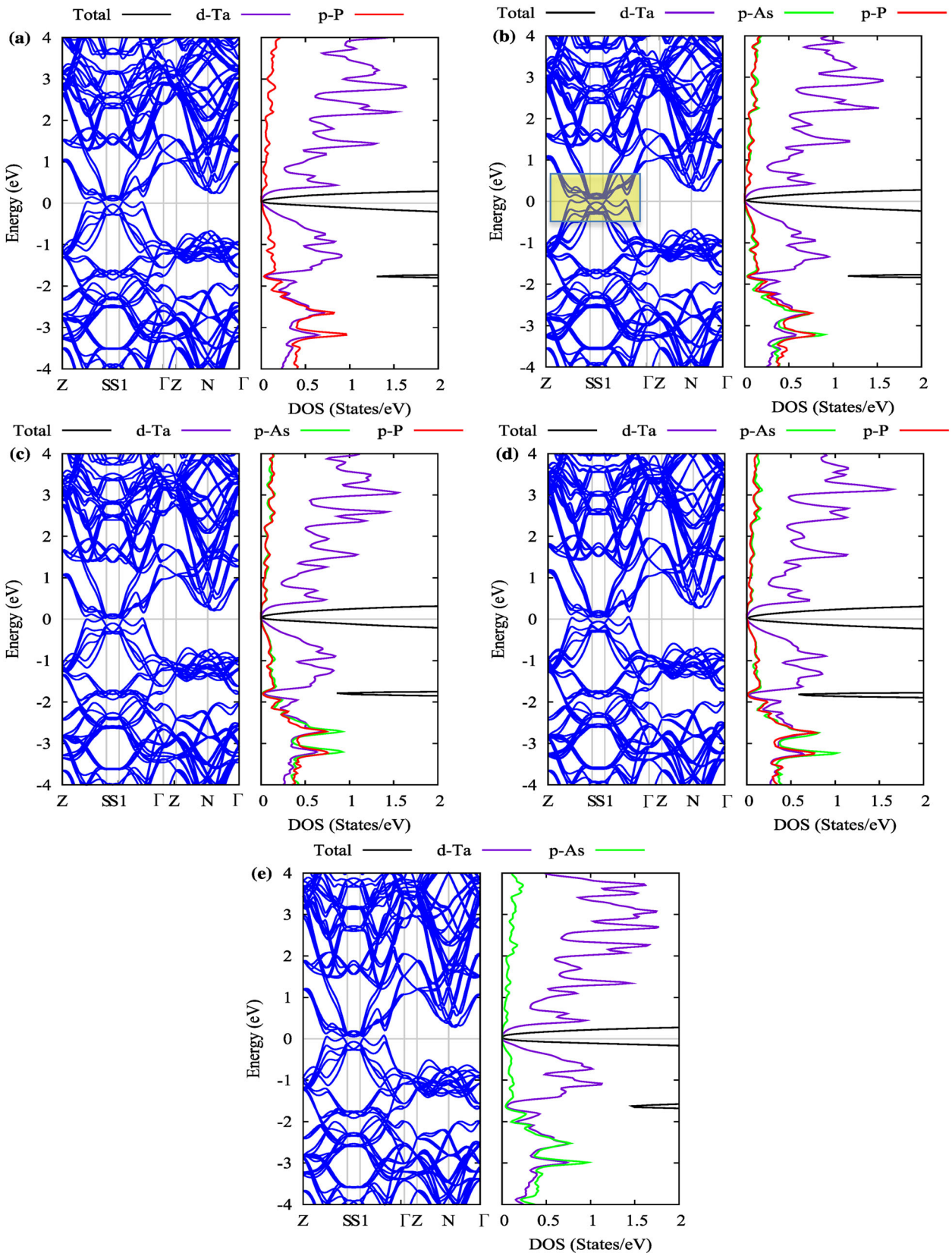

Figure 3. Band structure and density of states for the TaP_xAs_{1-x} alloys with SOC consideration, including a) TaAs, b) $TaP_{0.25}As_{0.75}$, where the valence and conduction bands are gapped in the Z-S-S1-Γ path (shown in yellow box), c) $TaP_{0.5}As_{0.5}$, d) $TaP_{0.75}As_{0.25}$, and e) TaP.

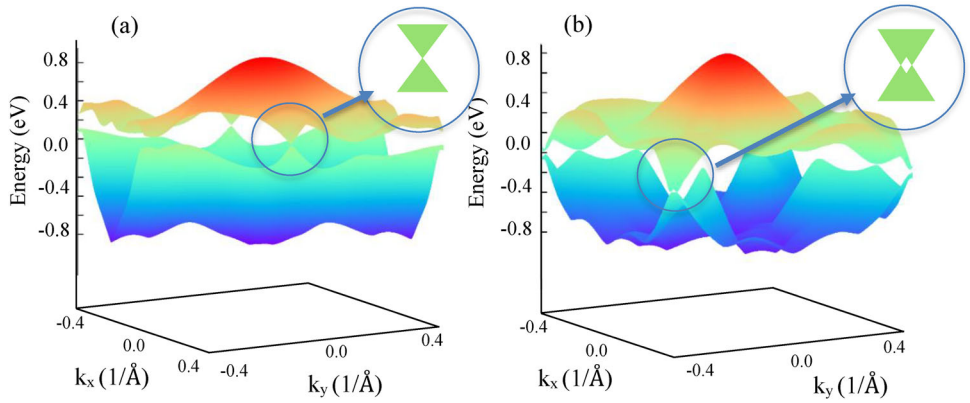

Figure 4. The band structure of TaP is shown in a 3D plot, highlighting the crossing points between the lowest valence band and the highest conduction band. a) The structure without SOC, and b) the structure with SOC consideration.

Calculations show six pairs of points for $x = 0$, seven pairs for $x = 0.25$, five pairs for $x = 0.50$, six pairs for $x = 0.75$, and four pairs for $x = 1.0$. In the presence of SOC, it is expected that the alloys will exhibit a different topological phase, with bandgaps opening at all the crossing points. However, searching for zero bandgaps in the presence of SOC, we found multiple zero-gap points with linear dispersion near the Fermi level in the first Brillouin zone. All zero gap points are twofold degenerate, which suggests the presence of Weyl points. **Figure 4**a displays the points and the corresponding cones of the TaP compound in the 3D plot of the lowest valence band and the highest conduction band near the Fermi level. The degenerate points for all alloys are near the Fermi level.

The inclusion of SOC is expected to result in a different topological phase for the alloys. The bandgaps of all alloys open at the crossing points, as depicted in Figure 4. Nevertheless, in our quest for zero bandgaps under the presence of SOC, we identified several zero-gap points with linear dispersion close to the Fermi level in the FBZ. These zero gap points are twofold degenerate, which suggests that they could be Weyl points.

Incorporating SOC effects into our calculations revealed that the previously fourfold degenerate points in the non-SOC cases are either gapped or split into two WPs, depending on the composition of the alloy. The number and positions of the WPs varied across the alloys. For instance, TaP compound had 12 WPs in the FBZ, with six at $k_z = 0$, two at $k_z = +0.2$, and two at $k_z = -0.2$, one at $k_z = +0.4$, and one at $k_z = -0.4$, with energy levels at $E = 0.0$ meV and $E = 5$ meV. The chirality of each WP was calculated using the WannierTools package, and all WPs were found to have a chirality of either +1 or −1, acting as the positive and negative magnetic monopoles, respectively, in the momentum space. Hence, all the alloys can be classified as WSMs with multiple WPs throughout the FBZ. The positions of the WPs were even functions of $\vec{k}$ due to the TRS and IS breaking. Thus, each WP had a partner in $-\vec{k}$ in the FBZ. Most WPs were closely spaced in the momentum space, and any perturbation could cause their movement and crossing, leading to their annihilation.

According to the bulk-edge correspondence, the presence of WPs induces topologically protected surface states, known as Fermi arcs.[11] The Fermi arcs originate and terminate at the projection of two or more WPs with different chirality on the surface of the FBZ. Currently, there are four distinct signatures for topological Fermi arcs.[46] The first signature is a Fermi arc where a surface state of constant energy contour makes an open curve that starts and ends at the projection of the WPs. The second signature is when multiple WPs project onto the same point, giving rise to a kink in the constant energy contour, which can only arise from the attachment of two Fermi arcs. The other two signatures are an odd set of closed contours and an even number of contours without kinks.

To probe the existence of the topological surface states of the TaP_xAs_{1-x} alloys, the surface projected band structure of the FBZ and the surface state spectrum on the (111) surface were calculated and inspected, as shown in **Figure 5**a–c for the TaP compound. The surface projected band structure on the (111) surface shows that the crossing points along the $\bar{z}$-$\bar{y}$ and $\bar{x}$-$\bar{\Gamma}$ paths are the WPs at the energy of 0.0 eV, while for the energy of 0.05 eV, only the crossing points along the $\bar{z}$-$\bar{y}$ path are the WPs. The Fermi arcs connect the projection of these WPs with opposite chirality on the (111) surface, as depicted in Figure 5b, c. The surface state spectrum on the (111) surface is calculated for the energies of $E = 0.0$ and 0.05 eV, which correspond to the energies of the investigated WPs in TaP (Figure 5a). These results provide strong evidence for the existence of topological Fermi arcs in the TaP_xAs_{1-x} alloys, supporting their topological nature as WSMs. The calculated positions of the 12 WPs in the TaP compound is shown in Figure 5d, and the table in Figure 5e shows the number of WPs for various TaP_xAs_{1-x} compounds. The highest number of WPs was found in $TaP_{0.5}As_{0.5}$ with 40 WPs, followed by $TaP_{0.25}As_{0.75}$ with 34 WPs, TaAs with 24 WPs, $TaP_{0.75}As_{0.25}$ with 20 WPs, and TaP with 12 WPs. The findings from the presented table demonstrate that the number of Weyl points in TaP_xAs_{1-x} alloys can vary significantly depending on the alloy composition. These results emphasize the crucial role of considering the alloy composition when searching for Weyl semimetals.

4. Conclusion

In conclusion, we have presented a detailed investigation of the structural, electronic, and topological properties of the TaP_xAs_{1-x} ($x = 0$, 0.25, 0.50, 0.75, 1) alloys by combining first-principles

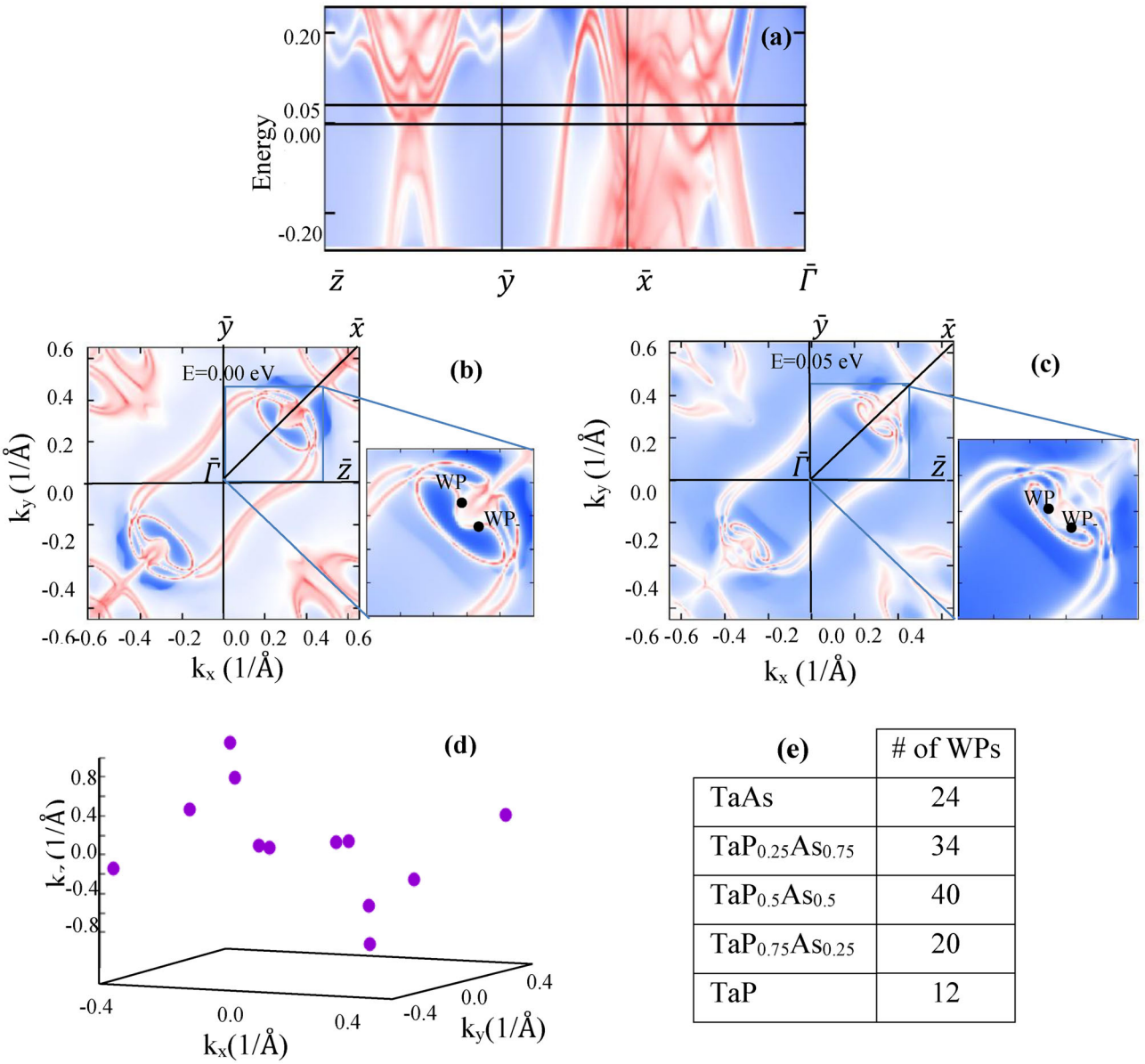

(e)	# of WPs
TaAs	24
$TaP_{0.25}As_{0.75}$	34
$TaP_{0.5}As_{0.5}$	40
$TaP_{0.75}As_{0.25}$	20
TaP	12

Figure 5. The topological properties of TaP compound. a) The surface state band structure of TaP on the (111) surface is plotted along the high symmetry $\vec{k}$ path. The energy values of 0.0 and 0.05 eV are shown with solid lines. The surface state spectrum of TaP on the (111) surface is shown for the energies of b) 0.0 eV and c) 0.05 eV with SOC consideration. The Fermi arcs, connecting the WPs of opposite chirality, are displayed in (b) and (c) with a zoomed-in view. d) The distribution of WPs in the FBZ reveals 12 with small separations. e) The number of WPs in each alloy.

calculations, using the WIEN2K package, and TB calculations, using the WANNIERTOOLS package. Our calculations reveal that the alloys possess multi-band crossings near the Fermi level due to band inversion, resembling DSMs when the SOC is neglected. However, the SOC consideration leads to the lifting of these degeneracies, and the alloys undergo a WSM phase with multiple WPs distributed throughout the FBZ. The calculated chirality of the WPs in all alloys is +1/−1, acting like the positive and negative magnetic monopoles in momentum space. Furthermore, the surface state spectrum presents Fermi arcs starting and ending on the projection of the WPs on the (111) surface. These results demonstrate the potential of the TaP_xAs_{1-x} alloys to serve as novel topological materials with applications in various fields such as spintronic and quantum computing. Our findings may also pave the way for further exploration and design of topological semimetals hosting fermionic quasiparticles.

Appendix

Weyl points (WPs) in the first Brillouin zone (FBZ) of TaP_xAs_{1-x} alloys are calculated and demonstrated in **Figure A1**. It can be seen that TaAs has 24 WPs, $TaP_{0.25}As_{0.75}$ 34, $TaP_{0.5}As_{0.5}$ 40, and $TaP_{0.75}As_{0.25}$ 20 in the FBZ. Among these compositions, $TaP_{0.5}As_{0.5}$ has the largest, and $TaP_{0.75}As_{0.25}$ has the smallest number of WPs. Most WPs have slight separations making closely coupled pairs.

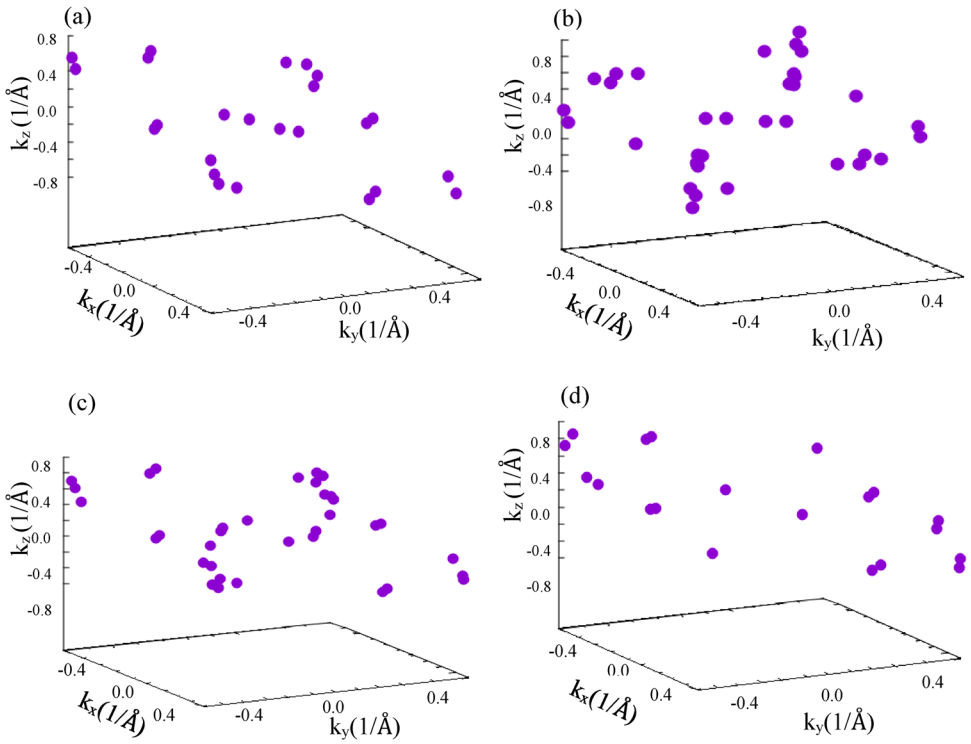

Figure A1. WPs in the FBZ of TaP_xAs_{1-x} alloys are shown. There are a) 24 pairs of WPs in TaAs, b) 34 in $TaP_{0.25}As_{0.75}$, c) 40 in $TaP_{0.5}As_{0.5}$, and d) 20 in $TaP_{0.75}As_{0.25}$.

Acknowledgements

D.V. acknowledges funding support from the National Science Foundation (NSF) under Grant No. CBET-2110603.

Conflict of Interest

The authors declare no conflict of interest.

Data Availability Statement

The data that support the findings of this study are available from the corresponding author upon reasonable request.

Keywords

density functional theory, Dirac semimetal, TaP_xAs_{1-x}, tight-binding method, topological materials, Weyl semimetal

Received: March 22, 2023
Revised: April 22, 2023
Published online: May 4, 2023

[1] S. Wang, B. C. Lin, A. Q. Wang, D. P. Yu, Z.-M. Liao, *Adv. Phys.: X* **2017**, *2*, 518.
[2] W. Witczak-Krempa, M. Knap, D. Abanin, *Phys. Rev. Lett.* **2014**, *113*, 136402.
[3] I. Belopolski, P. Yu, D. S. Sanchez, Y. Ishida, T. R. Chang, S. S. Zhang, S. Y. Xu, H. Zheng, G. Chang, G. Bian, *Nat. Commun.* **2017**, *8*, 942.
[4] A. Zyuzin, S. Wu, A. Burkov, *Phys. Rev. B* **2012**, *85*, 165110.
[5] T. L. Hughes, E. Prodan, B. A. Bernevig, *Phys. Rev. B* **2011**, *83*, 245132.
[6] Y. Zhang, Y. Sun, B. Yan, *Phys. Rev. B* **2018**, *97*, 041101.
[7] Z. Wang, Y. Sun, X. Q. Chen, C. Franchini, G. Xu, H. Weng, X. Dai, Z. Fang, *Phys. Rev. B* **2012**, *85*, 195320.
[8] S. Y. Xu, C. Liu, S. K. Kushwaha, R. Sankar, J. W. Krizan, I. Belopolski, M. Neupane, G. Bian, N. Alidoust, T. R. Chang, H. T. Jeng, C. Y. Huang, W. F. Tsai, H. Lin, P. P. Shibayev, F. C. Chou, R. J. Cava, M. Z. Hasan, *Science* **2015**, *347*, 294.
[9] B. Lv, S. Muff, T. Qian, Z. Song, S. Nie, N. Xu, P. Richard, C. E. Matt, N. C. Plumb, L. Zhao, *Phys. Rev. Lett.* **2015**, *115*, 217601.
[10] Z. Fang, N. Nagaosa, K. S. Takahashi, A. Asamitsu, R. Mathieu, T. Ogasawara, H. Yamada, M. Kawasaki, Y. Tokura, K. Terakura, *Science* **2003**, *302*, 92.
[11] Y. Lu, N. Jia, L. Su, C. Owens, G. Juzeliūnas, D. I. Schuster, J. Simon, *Phys. Rev. B* **2019**, *99*, 020302.
[12] P. Hosur, *Phys. Rev. B* **2012**, *86*, 195102.
[13] T. Ojanen, *Phys. Rev. B* **2013**, *87*, 245112.
[14] J. Y. Wu, W. P. Su, G. Gumbs, *Sci. Rep.* **2020**, *10*, 7674.
[15] H. Li, H. He, H. Z. Lu, H. Zhang, H. Liu, R. Ma, Z. Fan, S. Q. Shen, J. Wang, *Nat. Commun.* **2016**, *7*, 10301.
[16] X. Huang, L. Zhao, Y. Long, P. Wang, D. Chen, Z. Yang, H. Liang, M. Xue, H. Weng, Z. Fang, X. Dai, G. Chen, *Phys. Rev. X* **2015**, *5*, 031023.
[17] S. F. Zhang, C. W. Zhang, P. J. Wang, Q. F. Sun, *Sci. China: Phys., Mech. Astron.* **2018**, *61*, 117811.
[18] T. Schumann, M. Goyal, D. A. Kealhofer, S. Stemmer, *Phys. Rev. B* **2017**, *95*, 241113.
[19] A. Burkov, L. Balents, *Phys. Rev. Lett.* **2011**, *107*, 127205.
[20] W. Shi, L. Muechler, K. Manna, Y. Zhang, K. Koepernik, R. Car, J. Van Den Brink, C. Felser, Y. Sun, *Phys. Rev. B* **2018**, *97*, 060406.

[21] S. Y. Xu, N. Alidoust, I. Belopolski, Z. Yuan, G. Bian, T. R. Chang, H. Zheng, V. N. Strocov, D. S. Sanchez, G. Chang, *Nat. Phys.* **2015**, *11*, 748.
[22] S. Y. Xu, I. Belopolski, D. S. Sanchez, C. Zhang, G. Chang, C. Guo, G. Bian, Z. Yuan, H. Lu, T. R. Chang, P. P. Shibayev, M. L. Prokopovych, N. Alidoust, H. Zheng, C. C. Lee, S. M. Huang, R. Sankar, F. Chou, C. H. Hsu, H. T. Jeng, A. Bansil, T. Neupert, V. N. Strocov, H. Lin, S. Jia, M. Z. Hasan, *Sci. Adv.* **2015**, *1*, e1501092.
[23] H. Weng, C. Fang, Z. Fang, B. A. Bernevig, X. Dai, *Phys. Rev. X* **2015**, *5*, 011029.
[24] S. M. Huang, S. Y. Xu, I. Belopolski, C. C. Lee, G. Chang, B. Wang, N. Alidoust, G. Bian, M. Neupane, C. Zhang, *Nat. Commun.* **2015**, *6*, 7373.
[25] C. C. Lee, S. Y. Xu, S. M. Huang, D. S. Sanchez, I. Belopolski, G. Chang, G. Bian, N. Alidoust, H. Zheng, M. Neupane, *Phys. Rev. B* **2015**, *92*, 235104.
[26] B. Lv, H. Weng, B. Fu, X. P. Wang, H. Miao, J. Ma, P. Richard, X. Huang, L. Zhao, G. Chen, *Phys. Rev. X* **2015**, *5*, 031013.
[27] B. R. Rano, I. M. Syed, S. H. Naqib, *J. Alloys Compd.* **2020**, *829*, 154522.
[28] D. Bulmash, C. X. Liu, X. L. Qi, *Phys. Rev. B* **2014**, *89*, 081106.
[29] B. Singh, G. Chang, T. R. Chang, S. M. Huang, C. Su, M. C. Lin, H. Lin, A. Bansil, *Sci. Rep.* **2018**, *8*, 10540.
[30] S. Y. Xu, N. Alidoust, G. Chang, H. Lu, B. Singh, I. Belopolski, D. S. Sanchez, X. Zhang, G. Bian, H. Zheng, *Sci. Adv.* **2017**, *3*, e1603266.
[31] M. Zhang, G. Wang, *Comput. Mater. Sci.* **2020**, *171*, 109206.
[32] G. Wang, J. Wei, *Comput. Mater. Sci.* **2016**, *124*, 311.
[33] D. S. Sanchez, G. Chang, I. Belopolski, H. Lu, J. X. Yin, N. Alidoust, X. Xu, T. A. Cochran, X. Zhang, Y. Bian, *Nat. Commun.* **2020**, *11*, 3356.
[34] Q. Xu, E. Liu, W. Shi, L. Muechler, J. Gayles, C. Felser, Y. Sun, *Phys. Rev. B* **2018**, *97*, 235416.
[35] Y. Wu, D. Mou, N. H. Jo, K. Sun, L. Huang, S. L. Bud'ko, P. C. Canfield, A. Kaminski, *Phys. Rev. B* **2016**, *94*, 121113.
[36] H. Weng, X. Dai, Z. Fang, *J. Phys.: Condens. Matter* **2016**, *28*, 303001.
[37] P. Hohenberg, W. Kohn, *Phys. Rev.* **1964**, *136*, B864.
[38] P. Blaha, K. Schwarz, F. Tran, R. Laskowski, G. K. Madsen, L. D. Marks, *J. Chem. Phys.* **2020**, *152*, 074101.
[39] A. A. Mostofi, J. R. Yates, G. Pizzi, Y. S. Lee, I. Souza, D. Vanderbilt, N. Marzari, *Comput. Phys. Commun.* **2014**, *185*, 2309.
[40] Q. Wu, S. Zhang, H.-F. Song, M. Troyer, A. A. Soluyanov, *Comput. Phys. Commun.* **2018**, *224*, 405.
[41] J. P. Perdew, K. Burke, M. Ernzerhof, *Phys. Rev. Lett.* **1996**, *77*, 3865.
[42] A. Alexandradinata, X. Dai, B. A. Bernevig, *Phys. Rev. B* **2014**, *89*, 155114.
[43] D. Lee, J. Joannopoulos, *Phys. Rev. B* **1981**, *23*, 4997.
[44] S. Smidstrup, D. Stradi, J. Wellendorff, P. A. Khomyakov, U. G. Vej-Hansen, M. E. Lee, T. Ghosh, E. Jónsson, H. Jónsson, K. Stokbro, *Phys. Rev. B* **2017**, *96*, 195309.
[45] F. Murnaghan, *Proc. Natl. Acad. Sci. USA* **1944**, *30*, 244.
[46] M. Z. Hasan, S. Y. Xu, I. Belopolski, S.-M. Huang, *Annu. Rev. Condens. Matter Phys.* **2017**, *8*, 289.